

# **TomoNet: A streamlined cryoET software pipeline with automatic particle picking on flexible lattices**

Hui Wang<sup>1,2,3,\*</sup>, Shiqing Liao<sup>2,3</sup>, Xinye Yu<sup>3</sup>, Jiayan Zhang<sup>2,3</sup>, and Z. Hong Zhou<sup>1,2,3,\*</sup>

<sup>1</sup>Department of Bioengineering, University of California, Los Angeles (UCLA), Los Angeles, CA 90095, USA

<sup>2</sup>California NanoSystems Institute, UCLA, Los Angeles, CA 90095, USA

<sup>3</sup>Department of Microbiology, Immunology, and Molecular Genetics, UCLA, Los Angeles, CA 90095, USA

**\*Corresponding author:**

Z. Hong Zhou ([Hong.Zhou@UCLA.edu](mailto:Hong.Zhou@UCLA.edu), 1-310-694-7527)

## 1 **ABSTRACT**

2 Cryogenic electron tomography (cryoET) is capable of determining *in situ* biological structures of  
3 molecular complexes at near atomic resolution by averaging half a million subtomograms. While  
4 abundant complexes/particles are often clustered in arrays, precisely locating and seamlessly  
5 averaging such particles across many tomograms present major challenges. Here, we  
6 developed TomoNet, a software package with a modern graphical user interface to carry out the  
7 entire pipeline of cryoET and subtomogram averaging to achieve high resolution. TomoNet  
8 features built-in automatic particle picking and 3D classification functions and integrates  
9 commonly used packages to streamline high-resolution subtomogram averaging for structures  
10 in one-, two- or three-dimensional arrays. Automatic particle picking is accomplished in two  
11 complementary ways: one based on template matching and the other employing deep learning.  
12 TomoNet's hierarchical file organization and visual display facilitate efficient data management  
13 as required for large cryoET datasets. Applications of TomoNet to three types of datasets  
14 demonstrate its capability of efficient and accurate particle picking on flexible and imperfect  
15 lattices to obtain high-resolution 3D biological structures: virus-like particles, bacterial surface  
16 layers within cellular lamellae, and membranes decorated with nuclear egress protein  
17 complexes. These results demonstrate TomoNet's potential for broad applications to various  
18 cryoET projects targeting high-resolution *in situ* structures.

## 19 INTRODUCTION

20 Single-particle cryogenic electron microscopy (cryoEM) is employed to elucidate atomic-level  
21 structures of purified biological complexes. This methodology adheres to a standardized and  
22 well-established workflow supported by advanced software packages such as Relion<sup>1</sup> and  
23 cryoSparc<sup>2</sup>. In parallel, cryogenic electron tomography (cryoET), coupled with subtomogram  
24 averaging (STA), expands the investigative scope to encompass heterogeneous  
25 macromolecules in their native context<sup>3-10</sup>. To enhance the resolution of subunits within *in situ*  
26 macromolecules, subtomograms (*i.e.*, particles) are extracted from each tomogram and then  
27 subjected to 3D alignment and averaging, thereby improving signal-to-noise ratio. Notably, STA  
28 has achieved resolutions up to sub-3 Å for *in situ* structures of large cellular complexes such as  
29 ribosomes, approaching the capabilities of single-particle cryoEM methodologies<sup>11-14</sup>.

30 The workflow for cryoET and STA typically involves five key components across specific  
31 software packages. In cryoET preprocessing, dose fractionated frames are collected from an  
32 electron microscope, undergo motion correction, organized, and then assembled into individual  
33 tilt series. In tomogram reconstruction, three-dimensional reconstructions are generated from  
34 those tilt series. In particle picking, particles of interest are identified and extracted from  
35 tomograms. Complexity varies based on the diverse and intricate nature of *in situ* cellular  
36 samples and their unique configurations. Many packages include their own particle picking  
37 methods, such as oversampling using a supporting geometry in Dynamo<sup>15,16</sup>, template matching  
38 in emClarity<sup>17</sup> and machine learning in crYOLO<sup>18</sup>. In 3D refinement and classification, particles  
39 are iteratively classified and refined to obtain a final structure at sub-nanometer or near atomic  
40 resolution, which has been demonstrated by software packages like Relion<sup>13,19</sup>, emClarity<sup>17</sup>,  
41 EMAN2<sup>4</sup> and Warp<sup>20</sup>. Finally, activities in post-processing include map sharpening, Fourier shell  
42 correlation (FSC) calculation, visualization by placing averaged maps back into the original  
43 tomogram, etc. Users often need to navigate between several specialized software packages

44 for optimal results, which often demands a certain level of computational proficiency that poses  
45 a barrier for many.

46         The method for particle picking varies on a case-by-case basis, dictated by the  
47 characteristics of *in situ* cellular samples. In the early works of STA, manual particle picking was  
48 employed, particularly when aiming for resolutions between 20-50 Å with a maximum of several  
49 hundred particles<sup>21-23</sup>. However, for biological samples exhibiting periodic structures,  
50 oversampling on specified geometry was leveraged to significantly reduce the labor associated  
51 with acquiring enough particles for improved resolutions. For instance, HIV virus-like particles  
52 (VLPs) adopt a hexagonal Gag protein lattice in its sphere-like configuration<sup>16</sup>. Other examples  
53 include the Marburg Virus<sup>24</sup>, Herpes simplex virus<sup>25</sup>, and the Coat protein complex II<sup>26</sup>, all of  
54 which contain lattice-like arrangements with repeating subunits that could benefit from particle  
55 picking automation when performing cryoET data processing. With an increasing demand for  
56 automation to enhance efficiency with minimal manual intervention, template matching has  
57 emerged as a popular method for automatic particle picking, relying on a user-provided  
58 reference map<sup>17,27</sup>. Simultaneously, convolutional neural networks have shown promising  
59 results for cryoET automatic particle picking given its capacity to analyze three-dimensional  
60 feature maps and autonomously identify prominent features within specific samples<sup>28-31</sup>. These  
61 machine learning approach typically operate template-free and often obviates the need for  
62 human annotation<sup>32</sup>.

63         The expanding array of specialized software tools designed for specific tasks posts a  
64 critical need for seamless software integration within the cryoET workflow. Transitioning  
65 between various software packages can be a cumbersome process. Remarkably, recent  
66 initiatives have made notable progress in tackling this integration challenge. For example,  
67 TomoBEAR<sup>33</sup> offers an integrated solution, while ScipionTomo<sup>34</sup> and nextPYP<sup>35</sup> provide a  
68 comprehensive web-based platform for managing various tasks in the cryoET pipeline. Notably,

69 none of these packages takes specific advantage of the fact that abundant complexes exist in  
70 arrays of some sort, albeit with imperfections, variability, or flexibility.

71 In this context, we have developed TomoNet, a software package designed for  
72 streamlining the cryoET and STA data processing workflow, with a modern GUI ([Figure 1 and](#)  
73 [Figure 2](#)). Our methodology employs a geometric template matching approach, rooted in the  
74 concept of "Auto Expansion", which serves as a general particle picking solution for biological  
75 complexes organized in flexible, variable, or imperfect arrays. TomoNet is also powered by a  
76 deep learning-based solution to automate particle picking, which only needs 1-3 tomograms  
77 with known particle locations as ground truth for model training. Importantly, while TomoNet is  
78 particularly powerful for locating and averaging particles arranged on flexible or imperfect  
79 lattices, it can be applied to a broader range of particle types, offering a more generalizable  
80 trained model. These methods significantly diminish the need for manual inputs, and their  
81 outcomes can be seamlessly imported into Relion for subsequent high-resolution 3D  
82 classifications and refinements. We demonstrate the capabilities of TomoNet by applying it to  
83 three datasets with distinct protein lattice types, highlighting its accuracy and efficiency in  
84 identifying particles across diverse scenarios.

## 85 **RESULTS**

### 86 **Overall design of TomoNet**

87 TomoNet is a Python-based software package that integrates commonly used cryoET packages  
88 to streamline the cryoET and STA pipeline, with a particular emphasis on automating particle  
89 picking of lattice-configured structures and cryoET project management. As shown in the main  
90 menu and the entire TomoNet pipeline ([Figure 1 and Figure 2](#)), after data collection from  
91 electron microscopy, TomoNet can perform motion correction with integration of MotionCorr<sup>236</sup>;  
92 tilt series assembly and tomogram reconstruction with integration of IMOD<sup>37</sup> and AreTomo<sup>38</sup>;  
93 CTF estimation with integration of CTFFIND4<sup>39</sup>; manual particle picking with IMOD; particle

94 picking using built-in geometric template matching-based algorithms with integration of PEET<sup>40</sup>;  
95 automatic particle picking using built-in deep learning-based algorithms; 3D  
96 classification/particle cleaning and subtomograms placing back with built-in algorithms. This  
97 design also allows on-the-fly tomogram reconstruction processing during data collection, which  
98 facilitates a quick quality check. TomoNet generates particle picking results in STAR format<sup>41</sup>,  
99 which can be incorporated into Relion for high-resolution 3D refinement. It can also read Relion  
100 results in STAR format for particle cleaning and subtomograms placing back (Figure 1).

### 101 **Particle picking with “Auto Expansion”**

102 The “Auto Expansion” module is based on template matching and uses cross-correlation  
103 coefficient as a selection criterion, with a design to pick particles on flexible lattices with minimal  
104 manual inputs, its basic concept is elucidated in Figure 3. These particles exist in array-like  
105 configurations and manifest as flexible, partial, and imperfect lattices in one, two and three  
106 dimensions (1-3D). Examples are abound: microtubule doublets, ubiquitous in most cells,  
107 consist of 96 nm axonemal 1D translational repeat units<sup>22,42</sup> (1D rotational lattice); HIV VLPs<sup>43</sup>  
108 and surface layer (S-layer) lattice of prokaryotic cells<sup>44,45</sup> are composed of hexameric subunits  
109 (2D lattice); paraflagellar rod of protozoan species is organized into para-crystalline arrays in its  
110 distal zone<sup>21</sup> (3D lattice). In TomoNet, each of these isolated lattice densities is called a patch,  
111 within which all subunits of the complex are connected. For instance, Figure 3 illustrates two  
112 patches with different sizes.

113 “Auto Expansion” is an iterative process; each iteration expands the particle set by  
114 adding more unpicked ones. To initiate “Auto Expansion”, users need to prepare a few “seed”  
115 particles that sparsely distribute across all observed patches. Typically, the numbers of such  
116 “seed” particles per tomogram range from 20 to 200, which depends on the number and size of  
117 patches in the input tomogram. Then, “Auto Expansion” iteratively expands the “seed” particle  
118 set to a final particle set that contains all particles on given flexible lattices, following three steps

119 for each iteration (Figure 3). Firstly, potential particles adjacent to each “seed” particle are  
120 calculated and selected as “candidate” particles. Secondly, these “candidate” particles undergo  
121 alignments to a user-provided reference and are evaluated based on cross-correlation  
122 coefficient, such that “wrong” particles with low cross-correlations are excluded. Thirdly,  
123 qualified “candidate” particles are added to the particle set and become “seed” particles for the  
124 next iteration. During this process, only unpicked ones can be considered as “candidate”  
125 particles, and “Auto Expansion” stops either when no “candidate” particles are detected or when  
126 the user-defined maximum iteration number is reached. Doing this allows for an exhaustive  
127 exploration of particles on given lattices following their assembly topology with no restriction on  
128 geometry and outputs a final particle picking result (Figure 2).

129 Compared with conventional template matching methods, “Auto Expansion” incorporates  
130 prior knowledge of lattice configuration to iteratively guide the search for “candidate” particles,  
131 *i.e.*, unpicked particles following user-defined paths, as detailed in the Method section and  
132 TomoNet’s user manual. Thus, “Auto Expansion” significantly reduces computational complexity  
133 by searching in the regions of interest only, with restricted angular and translational search  
134 ranges defined by users. As a result, it reduces the number of incorrectly picked particles.  
135 Notably, “Auto Expansion” potentially works for any flexible, imperfect, or variable lattices in 1D,  
136 2D and 3D and has no intrinsic size limit of subunits.

### 137 **Automatic particle picking by deep learning**

138 The “AI AutoPicking” module is designed for automatic particle picking using supervised  
139 machine learning, which employs a U-net convolutional neural network for model training. There  
140 are three main steps in “AI AutoPicking”: training data preparation, neural network training, and  
141 particle coordinate prediction, as detailed in the Method section (Figure 4). It only requires an  
142 input training dataset consisting of 1-3 tomograms paired with their corresponding particles  
143 coordinate files. The trained model can then be applied on the entire tomography dataset and  
144 output predicted particles for each tomogram.

145           Essentially, the neural network in “AI AutoPicking” is trained as a voxel-wise binary  
146 classifier, which determines whether a voxel in density maps is part of a particle ([Figure 4b](#)). To  
147 prepare for training, data pairs (ground truth) consist of extracted subtomograms coupled with  
148 their associated segmentation maps, within where each particle is labeled by a cube near its  
149 center ([Figure 4a](#)). The trained neural network model can be applied on other tomograms to  
150 perform particle segmentation. Finally, the particles coordinate information can be retrieved from  
151 the predicted segmentation maps ([Figure 4c](#)).

### 152 **3D classification using TomoNet**

153 In addition to the above two commentary modules for particle picking, TomoNet allows users to  
154 eliminate “bad” particles based on user-defined geometric constraints, which could serve as 3D  
155 classification during high-resolution particle refinements. Lattice variation in cryoET data has  
156 multiple plausible causes. Biologically, particles may be incomplete near the lattice edge due to  
157 paused biology assembly process<sup>46</sup>. Experimentally, lattices tend to become flattened near the  
158 air-water interface of the sample during imaging. These variabilities pose challenges for 3D  
159 classification in the process of high-resolution STA, making it difficult to exclude “bad” particles  
160 that exhibit unexpected coordinates and orientations assignment as subunits of lattices  
161 ([Supplementary Movie 1](#)).

162           Removing these “bad” particles is necessary for achieving better resolutions<sup>47</sup>. To  
163 accomplish this, TomoNet assesses each particle by counting its neighboring particles and  
164 calculating the averaged tilt angle to these neighbors to represent local surface curvature of a  
165 lattice. TomoNet identifies particles with too few neighbors or large tilt angles to their neighbors  
166 as “bad” particles since they potentially deviate from the lattice configuration. This step can be  
167 integrated into high-resolution refinement in Relion, providing an alternative 3D classification  
168 method based on analyzing spatial relationships between particles.

### 169 **Application to *in situ* viral protein arrays: the matrix protein lattice in HIV VLPs**



170 To validate TomoNet as an integrated high-resolution cryoET and STA pipeline and an efficient  
171 particle picking tool, four tomograms were processed from the HIV-1 Gag dataset which  
172 resolved the Gag hexamer structure at 3.2 Å resolution. Motion corrected images underwent tilt  
173 series assembly, CTF estimation, and tomographic reconstruction using TomoNet. Within these  
174 tomograms, the VLP hexagonal lattice and its building blocks were observed, and some of  
175 these observed VLPs exhibited sphere-like geometry (Figure 5a).

176 As detailed in the Method section, a combination of “Auto Expansion” and “AI  
177 AutoPicking” was applied on the above four tomograms; as a result, particles were readily  
178 picked on all the observed lattice patches (Figure 5b, c). Then, these picked particles were  
179 imported to Relion to perform high-resolution particle refinements, resulting in a final  
180 reconstruction of the Gag hexamer structure (Figure 6).

181 Using the “3D subtomogram place back” function in TomoNet, 3D visualizations were  
182 generated to illustrate the *in situ* assembly of the VLP lattices (Figure 5d and Figure 7). All VLP  
183 lattices with various sizes and shapes were captured even with irregular shapes (Figure 7e and  
184 Supplementary Movie 2), demonstrated TomoNet’s particle picking ability on flexible lattices.  
185 Lattice defects on each VLP were also identified consistent with previous studies<sup>48</sup>, enhancing  
186 the understanding of lattice assembly mechanisms<sup>49</sup>.

### 187 **Application to focused ion beam (FIB)-milled cellular sample: the S-layer lattice of** 188 **prokaryotic cell**

189 We validated TomoNet’s particle picking capability by processing one tomogram of FIB-milled  
190 *Caulobacter crescentus* cells from EMD-23622<sup>50</sup>. The S-layer functions as a component of the  
191 cell wall covering the cell body. Thus, its lattice geometry is typically defined by the shape of  
192 cells (Figure 8a). The pleomorphic shape of *C. crescentus* cell in variable sizes, with the low  
193 contrast shown in this tomogram, hindered locating subunits on the S-layer lattice and raised  
194 difficulty for efficient particle picking on its S-layer lattice (Figure 8a).

195 TomoNet overcame the above challenges by utilizing the hexagonal configuration of S-  
196 layer lattices. With a minimal manual input, “Auto Expansion” picked over a thousand hexamer  
197 S-layer subunits. The intermediate STA result clearly reveals the hexagonal distribution of S-  
198 layer inner domains (Figure 8b). Visualization of S-layer lattices also shows that the picked  
199 particles were arranged in the expected hexagonal pattern, confirming the reliability and  
200 applicability of TomoNet as a particle picking tool (Figure 8c) and its broad application to  
201 structure determination of prokaryotic and archaeal cell walls<sup>45,51</sup>.

### 202 **Application to *in vitro* assembled arrays: nuclear egress complex (NEC) lattice**

203 We further validated TomoNet as an integrated high-resolution STA pipeline and an efficient  
204 particle picking tool by processing samples containing NEC lattices within budded vesicles.  
205 Nuclear egress is a pivotal step in herpes virus replication, driven by NEC and responsible for  
206 translocating nascent viral particles from nucleus to cytoplasm. In our reported dataset<sup>52</sup>, NEC  
207 heterodimers budded into large vesicles with diameters ranging from 100 nm to 500 nm, forming  
208 beehive-like lattices on the inner surface of these vesicles (Figure 9a, b). Because of their large  
209 sizes, noticeable compressions were observed during the sample freezing, reshaping the  
210 vesicles and NEC lattices from spherical to flattened disk shapes (Figure 9a, b). This  
211 conformational change was a consequence of the limitation in ice thickness imposed by cryoET,  
212 which restricts the sample thickness to approximately 250 nm, consequently posing challenges  
213 for particle picking.

214 TomoNet successfully picked NEC hexamer subunits following the topology of lattices.  
215 The intermediate STA result generated in TomoNet already showed the six heterodimers within  
216 one hexamer subunit (Figure 9c). With these picked particles, high-resolution 3D classifications  
217 and refinements were carried out to obtain a final reconstruction of NEC hexamer subunit at 5.4  
218 Å resolution, without preferred orientation bias (Figure 9c, d and Figure 6c), and all the helices  
219 were well resolved (Figure 9e). Visualization of subtomograms placing back shows that the  
220 large vesicle was compressed during sample freezing which stretched the NEC lattice, making it

221 appears flat and split at the air-water interface, while the middle part of the lattice appears to be  
222 more curved.

### 223 **Application to other types of arrays and free-floating particles**

224 The above examples show how TomoNet's ability to locate particles arrays arranged on flexible  
225 spheres (HIV), cell surfaces (S-layer) and nuclear membranes (NEC), which can be considered  
226 as topologically 2D lattices. In our published work of various cryoET structures, TomoNet has  
227 also been used to locate subtomograms arranged on flexible filaments (*i.e.*, 1D arrays) such as  
228 the flagella of *Trypanosoma brucei*<sup>22,42</sup> and the amyloid-like sheath protein on  $\beta$ -hoops of the  
229 prototypical archaeon, *Methanospirillum hungatei*<sup>53</sup>. In the case of 3D lattices, TomoNet has  
230 been also used to obtain the paraflagellar rod structure of *T. brucei*<sup>21</sup>. Since TomoNet has  
231 integrated packages and is designed for the entire cryoET and STA data processing pipeline, it  
232 can also be used as a general-purpose package for subtomogram averaging towards high  
233 resolution when particles are free floating and without local order. In the latter case, TomoNet  
234 would have the same limitation recognized for all other cryoET software packages, that is, high  
235 resolution is currently only achieved for large complexes, such as ribosomes.

## 236 **DISCUSSION**

237 In this paper, we report the implementation and application of TomoNet and demonstrate its  
238 efficacy in particle picking across three distinct datasets featuring particles with varying lattice  
239 configurations. TomoNet stands out as the first software to exhaustively trace lattices following  
240 its inherent topology. This unique approach ensures that the particle picking results faithfully  
241 reflect *in situ* or *in vitro* lattice shape, providing valuable insights into how these lattices are  
242 formed by their constituent subunits. For HIV VLPs, TomoNet application enabled us to directly  
243 visualize the VLPs lattices and their defects potentially caused by the absence of pentamer  
244 subunits. Similarly, for the NEC dataset, TomoNet facilitated a more direct observation of lattice  
245 conformation changes resulting from the sample freezing process. Since vesicles in this dataset

246 were too large to be compressed from a sphere into a disk-like shape, the lattice regions near  
247 the air-water interface became stretched and subsequently divided into smaller fragments.  
248 Moreover, TomoNet demonstrated its exceptional performance, even when dealing with  
249 datasets characterized by extremely low contrast. For instance, in the cellular S-layer tomogram  
250 of a lamella, S-layer subunits were nearly imperceptible to human observations. Therefore,  
251 "Auto Expansion" excelled in particle picking without requiring denoising or contrast-  
252 enhancement algorithms.

253         Additionally, "AI AutoPicking", the deep learning-based module, demonstrated excellent  
254 performance on automatic particle picking, showing potential in handling a wide range of particle  
255 types even beyond those with lattice-like arrangements. Compared to the template matching-  
256 based "Auto Expansion", "AI AutoPicking" has several advantages in particle picking. Firstly, it  
257 applies to particles situated on flexible lattices and those arranged in scattered patterns, such as  
258 cellular ribosomes. The neural network learns to pick by discerning 3D features of individual  
259 particles, and it does not require prior knowledge about lattice configuration. Secondly, it utilizes  
260 GPUs for fast convolution operations, enabling particle prediction in just several minutes for  
261 each tomogram. Thirdly, it does not require the "seed" particles used in "Auto Expansion", which  
262 further reduces human efforts by approximately 5-15 minutes per tomogram. This is especially  
263 beneficial for processing extensive tomography datasets with hundreds of tomograms.  
264 However, comparing their final output particles, "AI AutoPicking" typically picks fewer particles  
265 than "Auto Expansion" because it misses certain particles on the flexible lattices. Thus, these  
266 two modules are complementary to each other and can be incorporated to further explore these  
267 missing particles.

268         Regarding the pipeline design, each module within TomoNet is designed to be highly  
269 independent, ensuring flexibility for integrating future methods and third-party packages. This  
270 adaptable framework positions TomoNet as a platform of choice for other developers to build  
271 their own innovations. At present, TomoNet is primarily tailored for integration with the Relion-

272 related pipeline. However, it can accommodate specific demands and can be extended to  
273 integrate other pipelines, including emClarity<sup>17</sup>, EMAN2<sup>4</sup>, M<sup>54</sup>, and others in the future. In  
274 summary, TomoNet significantly simplifies the overall process for users in managing and  
275 monitoring every step of the complete cryoET and STA pipeline. Its user-friendly GUI design  
276 notably reduces the entry barrier for newcomers to the fast-emerging cryoET field. The particle  
277 picking modules of TomoNet provide a general solution for particles organized in lattice-like  
278 arrangements, ensuring both accuracy and efficiency, thereby facilitating the high-resolution  
279 STA pipeline.

## 280 **METHODS**

281 TomoNet is an open-source software package developed using Python. It follows a highly  
282 modularized architecture with each module responsible for specific tasks in a typical cryoET and  
283 STA data processing pipeline. Modules in TomoNet mainly cover the upper stream of the  
284 cryoET and STA pipeline including procedures of motion correction, tilt series generation,  
285 tomogram reconstruction, CTF estimation and particle picking, while leave the high-resolution  
286 3D refinement to established software package like Relion ([Figure 1](#)). The design of a modern  
287 GUI, established with PyQt5 platform, enhances user-friendliness, and helps with tracking the  
288 processing progress ([Figure 2](#)). With table views, users can obtain a comprehensive overview of  
289 the entire dataset, facilitating direct and intuitive management for each tomogram ([Figure 2](#)).

### 290 **Implementation of modules for motion correction, tomogram reconstruction and CTF** 291 **estimation**

292 Motion correction, tomogram reconstruction, and CTF estimation related functions are  
293 organized into individual modules in TomoNet, with the integration of corresponding external  
294 software packages including MotionCorr2<sup>36</sup>, IMOD<sup>37</sup> or AreTomo<sup>38</sup> and CTFFIND4<sup>39</sup>,  
295 respectively. Since their codes are not rewritten in TomoNet, users have to install each of them  
296 before using the corresponding modules.

297           The “Motion Correction” module is used to correct beam-induced sample motion. It  
298 requires an input folder path that contains all the dose fractionated frames, then user can  
299 specify their MotionCorr2 parameters in the GUI. After clicking the “RUN” button, TomoNet will  
300 perform motion correction for all the input images and save the results in a separated directory.  
301 This module also allows on-the-fly motion correction during data collection.

302           The “3D Reconstruction” module comprises two sub-functions: “TS Generation” and  
303 “Reconstruction”. Within “TS Generation”, users can readily assemble tilt series for each  
304 tomogram from the previously generated motion corrected images. It provides advanced options  
305 for data cleaning, such as setting a minimum acceptable number of tilt images for a tomogram,  
306 removing duplicate images at the same tilt angle by excluding images with older time stamps.  
307 The “Reconstruction” tab automatically reads and lists all tomograms in a table view, with  
308 essential information, such as tilt image number and alignment errors, and action buttons for  
309 restart, continue and delete individual tomogram reconstruction process. This simplifies the  
310 assessment of reconstruction results and facilitating tomogram reconstruction management.

311           The “CTF Estimation” module is used for the tilt series defocus estimation, with support  
312 of parallel processing using multiple CPUs. Its outcomes are also listed in a table view with  
313 visualization features, such as displaying defocus at 0 degree and plotting the defocus  
314 distribution across all tilt angles.

### 315 **Implementation of the “Manual Picking” module**

316           The “Manual Picking” module is designed for general management of manual particle picking,  
317 especially for the preparation of “seed” particles required in “Auto Expansion”. IMOD stalknit  
318 picking criteria is implemented to define the Y-axis for each particle with 2 points, and the center  
319 in between them. In the example of HIV dataset, 5-10 particles were manually picked as the  
320 “seed” particles for each VLP lattice, which only takes several minutes per tomogram ([Figure](#)  
321 [5a](#)).

### 322 **Design and implementation of the “Auto Expansion” module**

323 “Auto Expansion” consists of three steps as shown in [Figure 2](#). “Generate tomograms.star” is  
324 used to generate a STAR format file that maintain information of tomograms and their  
325 associated “seed” particles to be applied in “Auto Expansion”. “Generate Picking Parameter” is  
326 used to set up parameters required for particle set expansion through the described iterative  
327 process. The parameters include angular search ranges and steps, translational search ranges  
328 and steps, a “transition list” (explained later), box size used in particle alignment, distance  
329 between neighboring repeating subunits, reference and mask map, cross-correlation threshold,  
330 etc. The “transition list” is customized by users to describe the targeting lattice configuration,  
331 with each transition denoted by  $[sx, sy, sz]$ , where  $sx$ ,  $sy$  and  $sz$  are translational shifts from the  
332 center of “seed” particle to one of its neighbors along X, Y and Z-axis, respectively. Thus, “Auto  
333 Expansion” can use it to guide the search of “candidate” particles. These user defined  
334 parameters will then be saved into a JSON format file. “Run Particle Expansion” takes the  
335 above STAR and JSON format files as inputs to perform the iterative particle set expansion.

336 During the “Auto Expansion” processing, three directories will be generated for each  
337 tomogram. They are “*TomoName*” as the working directory for carrying out the current iteration,  
338 “*TomoName\_cache*” that stores intermediate results from finished iterations, and  
339 “*TomoName\_final*” that stores the final particle picking results. The iteration number of “Auto  
340 Expansion” is typically greater than one. However, “Auto Expansion” allows for some special  
341 usage cases. For example, in the scenario when users need to modify the particle picking  
342 setting such as a different cross-correlation threshold, user can generate the new picking  
343 parameter file, then execute “Run Particle Expansion” by setting the iteration number as 0. This  
344 prompts the program to skip the “candidate” searching steps, but just gather all intermediate  
345 results saved in “*TomoName\_cache*” directories, then generate a new “*TomoName\_final*” result.

### 346 **Design and implementation of the “AI AutoPicking” module**

347 The “AI AutoPicking” module comprise 3 main steps, “Prepare Training Dataset”, “Train Neural  
348 Network” and “Predict Particles coordinates”. It uses supervised machine learning that requires

349 users to provide ground truth, *i.e.*, tomogram with the associated particle coordinates files, for  
350 the model training. In this study, the ground truth data were prepared by “Auto Expansion”.

351 In “Prepare Training Dataset”, extracted subtomograms are used as inputs to the  
352 network training model for two reasons. Firstly, the size of tomogram used for picking is typically  
353 around 1000x1000x1000 voxels which is not applicable to be loaded in the GPU memory, but  
354 the size of extracted subtomograms is under 100x100x100 voxels. Secondly, it helps with  
355 increasing the number of training data pairs to avoid over-fitting during the network training. For  
356 the model output, the particle coordinates information was embedded into 3D binary  
357 segmentation maps, where the voxels associated with particles were set to 1, otherwise set to 0  
358 (Figure 4a).

359 In “Train Neural Network”, the above extracted subtomograms paired with their  
360 associated segmentation maps are used to train a neural network model to be a binary classifier  
361 that predict whether a voxel is near the center of a particle. The network architecture employed  
362 is derived from the one used in IsoNet<sup>46</sup> as it is well-suited for capturing generalized features of  
363 3D objects (Figure 4b). Since the learning task is voxel-wisely binary classification, cross  
364 entropy loss function is used instead of minimum squared error (MSE). Equipped with one RTX  
365 3080Ti graphic card, the training process can be completed swiftly within 1-2 hours if using the  
366 default parameters.

367 In “Predict Particles coordinates”, users can apply the trained model on the entire  
368 tomography dataset for particle coordinate prediction (Figure 4c). For each tomogram, TomoNet  
369 generate a predicted segmentation map first, then its particle coordinates information can be  
370 retrieved from the segmentation map by utilizing the hierarchical clustering algorithm from *scipy*  
371 module in Python.

### 372 **Implementation of tools within the “Other Utilities” module**

373 The “Other Utilities” module consists of two sub-functions: "Recenter | Rotate | Assemble  
374 to .star file" and "3D Subtomogram Place Back" as useful tools for post particle picking



375 processing. The first one allows users to assemble and convert the particle picking results into a  
376 STAR format file following the Relion4 convention, reset particles center to its symmetric center,  
377 and align the rotation axis to Relion Z-axis. The second one takes a user-provided STAR format  
378 file that contains particles information as input, then generates a ChimeraX<sup>55</sup> session file for 3D  
379 subtomograms placing back and a clean version of STAR format file with “bad” particles  
380 removed. This not only allows users to validate the accuracy of particle picking before importing  
381 into Relion, but also enables direct observation of the distribution and configuration of subunits  
382 after the high-resolution 3D refinements, providing overall *in situ* lattice observations (Figure 7).

### 383 **Processing tomograms of HIV VLP dataset**

384 The HIV VLP dataset was downloaded from the Electron Microscopy Public Image Archive  
385 (EMPIAR) with the accession code EMPIAR-10164<sup>43</sup>. Four tilt series, TS\_01, TS\_43, TS\_45  
386 and TS\_54, were used in this study. Downloaded micrographs were loaded into the TomoNet  
387 pipeline to perform tilt series assembly, CTF estimation, and tomogram reconstruction using the  
388 WBP algorithm.

389 Four-time binned tomograms with 5.4 Å pixel size were used for further particle picking.  
390 Firstly, tomograms TS\_01 and TS\_43 were used for “seed” particles preparation on 3 selected  
391 VLPs per tomogram, and an initial reference map was generated by averaging them in PEET.  
392 Secondly, one run of “Auto Expansion” was applied on the above two tomograms to get more  
393 particles, such as to refine the reference. Thirdly, with an improved reference, a new run of  
394 “Auto Expansion” was applied on the selected 3 VLPs in both tomogram (Figure 5b), then the  
395 particle picking result was used for neural network training in “AI AutoPicking”. Fourthly, after  
396 the particle prediction on all four tomograms with a trained model, “AI AutoPicking” produced  
397 4,860, 3,704, 4,550 and 2,101 particles for tomograms TS\_01, TS\_43, TS\_45 and TS\_54, as  
398 shown in Figure 5c. Lastly, the predicted particles were input as “seed” particles for the final run  
399 of “Auto Expansion”, resulting in 5,765, 4,043, 5,006, and 2,838 particles for tomograms TS\_01,

400 TS\_43, TS\_45 and TS\_54, which were imported into Relion to perform high-resolution  
401 refinements.

402         Following the same procedure carried out in the Relion4 tutorial together with TomoNet  
403 3D classification, the Gag hexamer structure was resolved at 3.2 Å resolution with 13,558  
404 particles from four tomograms. Resolution was calculated in Relion and on 3DFSC Processing  
405 Server<sup>56</sup>. The global resolution reported is based on the “gold standard” refinement procedures  
406 and the 0.143 Fourier shell correlation (FSC) criterion (Figure 6).

#### 407 **Processing one tomogram of *C. Crescentus* S-layer**

408 The FIB-milled *C. crescentus* data of one reconstructed tomogram was downloaded from  
409 Electron Microscopy Data Bank (EMDB) with the accession code EMD-23622<sup>50</sup>. This tomogram  
410 was directly used for “seed” particles preparation on two of the cells. Around 30 “seed” particles  
411 were manually picked and averaged using PEET to generate an initial reference map. “Auto  
412 Expansion” was applied on the “seed” particles for 5 iterations to get more particles such as to  
413 refine the reference map. With the improved reference map, another run of “Auto Expansion”  
414 was applied to the same “seed” particles for 15 iterations to search all particles on the outer  
415 surface of the cells, and finally yielded ~1,500 S-layer particles of hexamer subunits (Figure 8c).

#### 416 **Processing tomograms of NEC budding *in vitro***

417 The cryoET grid preparation and data collection were previously described<sup>52</sup>. Motion correction,  
418 tomogram reconstruction and CTF estimation were performed using TomoNet. Around 50-150  
419 “seed” particles were manually picked for each tomogram. “Auto Expansion” were applied on a  
420 total of 35 tomograms and yield the ~48,000 particles before Relion refinements. Following one  
421 round of 3D auto-refine job under four-binned pixel size and several rounds of 3D auto-refine  
422 jobs under two-binned pixel size and one round of 3D auto-refine under unbinned pixel size,  
423 together with TomoNet 3D classifications, the NEC hexamer structure was resolved at 5.4 Å  
424 resolution with totally 35,039 particles.

#### 425 **3D visualization**

426 IMOD<sup>37</sup> was used to visualize the 2D tomographic and segmentation map slices. UCSF  
427 ChimeraX<sup>55</sup> was used to visualize the STA results and the lattices generated by 3D  
428 subtomogram place back. The atomic models were fitted into the density map using the “fit in  
429 map” tool in ChimeraX.

## 430 **AVAILABILITY**

431 TomoNet code is available on Github website at <https://github.com/logicvay2010/TomoNet>, with  
432 a user manual. For the HIV VLPs dataset, the raw data was downloaded from the Electron  
433 Microscopy Public Image Archive (EMPIAR) with accession code EMPIAR-10164<sup>43</sup>, the Gag  
434 atomic model was downloaded from the Protein Data Bank (PDB) with accession code 5L93<sup>43</sup>.  
435 For the *C. Crescentus* S-layer dataset, the reconstructed tomogram was downloaded from the  
436 Electron Microscopy Data Bank (EMDB) with accession code EMD-23622<sup>50</sup>, and the subunit  
437 model was generated using atomic model with PDB accession code 6P5T<sup>57</sup>. The STA result of  
438 NEC hexamer is from EMDB with accession code EMD-40224<sup>52</sup>. The other data that support  
439 the findings of this study are available from the corresponding authors upon reasonable request.

## 440 **ACKNOWLEDGEMENTS**

441 We thank Elizabeth Draganova and Ekaterina Heldwein for the NEC dataset. This project is  
442 supported by grants from the US National Institutes of Health (GM071940 to Z.H.Z.) and the  
443 National Science Foundation (DMR-1548924 to Z.H.Z.).

## 444 **AUTHORSHIP CONTRIBUTIONS**

445 HW and ZHZ initialized and ZHZ supervised research; HW wrote the code and developed the  
446 software GUI with help from SL; HW, SL and XY tested the software on different datasets; HW,  
447 and ZHZ wrote the manuscript; JZ and XY assisted the manuscript writing; all authors reviewed  
448 and approved the paper.

## 449 **COMPETING INTERESTS STATEMENT**

450 The authors declare that there is no conflict of interest.

## 451 REFERENCES

- 452 1 Kimanius, D., Dong, L., Sharov, G., Nakane, T. & Scheres, S. H. W. New tools for automated  
453 cryo-EM single-particle analysis in RELION-4.0. *Biochem J* **478**, 4169-4185,  
454 doi:10.1042/BCJ20210708 (2021).
- 455 2 Punjani, A., Rubinstein, J. L., Fleet, D. J. & Brubaker, M. A. cryoSPARC: algorithms for rapid  
456 unsupervised cryo-EM structure determination. *Nat Methods* **14**, 290-296,  
457 doi:10.1038/nmeth.4169 (2017).
- 458 3 Wan, W. & Briggs, J. A. Cryo-Electron Tomography and Subtomogram Averaging. *Methods*  
459 *Enzymol* **579**, 329-367, doi:10.1016/bs.mie.2016.04.014 (2016).
- 460 4 Chen, M. *et al.* A complete data processing workflow for cryo-ET and subtomogram averaging.  
461 *Nat Methods* **16**, 1161-1168, doi:10.1038/s41592-019-0591-8 (2019).
- 462 5 Zhang, P. Advances in cryo-electron tomography and subtomogram averaging and classification.  
463 *Curr Opin Struct Biol* **58**, 249-258, doi:10.1016/j.sbi.2019.05.021 (2019).
- 464 6 Castano-Diez, D. & Zanetti, G. In situ structure determination by subtomogram averaging. *Curr*  
465 *Opin Struct Biol* **58**, 68-75, doi:10.1016/j.sbi.2019.05.011 (2019).
- 466 7 Hong, Y., Song, Y., Zhang, Z. & Li, S. Cryo-Electron Tomography: The Resolution Revolution and  
467 a Surge of In Situ Virological Discoveries. *Annu Rev Biophys* **52**, 339-360, doi:10.1146/annurev-  
468 biophys-092022-100958 (2023).
- 469 8 Huang, Y., Zhang, Y. & Ni, T. Towards in situ high-resolution imaging of viruses and  
470 macromolecular complexes using cryo-electron tomography. *J Struct Biol* **215**, 108000,  
471 doi:10.1016/j.jsb.2023.108000 (2023).
- 472 9 Sibert, B. S. *et al.* Workflow for High-resolution Sub-volume Averaging from Heterogenous Viral  
473 and Virus-like Assemblies. *Microsc Microanal* **29**, 943-944, doi:10.1093/micmic/ozad067.470  
474 (2023).
- 475 10 Kopylov, M., Bobe, D., Johnston, J. D. & Paraan, R. M. Modern Tools for In-situ Tomography.  
476 *Microsc Microanal* **29**, 954-955, doi:10.1093/micmic/ozad067.476 (2023).
- 477 11 Ni, T. *et al.* High-resolution in situ structure determination by cryo-electron tomography and  
478 subtomogram averaging using emClarity. *Nat Protoc* **17**, 421-444, doi:10.1038/s41596-021-  
479 00648-5 (2022).
- 480 12 Xue, L. *et al.* Visualizing translation dynamics at atomic detail inside a bacterial cell. *Nature* **610**,  
481 205-211, doi:10.1038/s41586-022-05255-2 (2022).
- 482 13 Zivanov, J. *et al.* A Bayesian approach to single-particle electron cryo-tomography in RELION-  
483 4.0. *Elife* **11**, doi:10.7554/eLife.83724 (2022).
- 484 14 Obr, M. & Schur, F. K. M. in *Advances in Virus Research* Vol. 105 (ed Félix A. Rey) 117-159  
485 (Academic Press, 2019).
- 486 15 Castano-Diez, D., Kudryashev, M., Arbeit, M. & Stahlberg, H. Dynamo: a flexible, user-friendly  
487 development tool for subtomogram averaging of cryo-EM data in high-performance computing  
488 environments. *J Struct Biol* **178**, 139-151, doi:10.1016/j.jsb.2011.12.017 (2012).
- 489 16 Scaramuzza, S. & Castaño-Díez, D. Step-by-step guide to efficient subtomogram averaging of  
490 virus-like particles with Dynamo. *PLOS Biology* **19**, e3001318, doi:10.1371/journal.pbio.3001318  
491 (2021).
- 492 17 Himes, B. A. & Zhang, P. emClarity: software for high-resolution cryo-electron tomography and  
493 subtomogram averaging. *Nature Methods* **15**, 955-961, doi:10.1038/s41592-018-0167-z (2018).
- 494 18 Wagner, T. *et al.* SPHIRE-crYOLO is a fast and accurate fully automated particle picker for cryo-  
495 EM. *Commun Biol* **2**, 218, doi:10.1038/s42003-019-0437-z (2019).
- 496 19 Bharat, T. A. M. & Scheres, S. H. W. Resolving macromolecular structures from electron cryo-  
497 tomography data using subtomogram averaging in RELION. *Nature Protocols* **11**, 2054-2065,  
498 doi:10.1038/nprot.2016.124 (2016).
- 499 20 Tegunov, D. & Cramer, P. Real-time cryo-electron microscopy data preprocessing with Warp.  
500 *Nature Methods* **16**, 1146-1152, doi:10.1038/s41592-019-0580-y (2019).
- 501 21 Zhang, J. *et al.* Structure of the trypanosome paraflagellar rod and insights into non-planar  
502 motility of eukaryotic cells. *Cell Discov* **7**, 51, doi:10.1038/s41421-021-00281-2 (2021).

- 503 22 Imhof, S. *et al.* Cryo electron tomography with volta phase plate reveals novel structural  
504 foundations of the 96-nm axonemal repeat in the pathogen *Trypanosoma brucei*. *eLife* **8**, e52058,  
505 doi:10.7554/eLife.52058 (2019).
- 506 23 Si, Z. *et al.* Different functional states of fusion protein gB revealed on human cytomegalovirus by  
507 cryo electron tomography with Volta phase plate. *PLOS Pathogens* **14**, e1007452,  
508 doi:10.1371/journal.ppat.1007452 (2018).
- 509 24 Bharat, T. A. *et al.* Cryo-electron tomography of Marburg virus particles and their morphogenesis  
510 within infected cells. *PLoS Biol* **9**, e1001196, doi:10.1371/journal.pbio.1001196 (2011).
- 511 25 Grünewald, K. *et al.* Three-dimensional structure of herpes simplex virus from cryo-electron  
512 tomography. *Science* **302**, 1396-1398, doi:10.1126/science.1090284 (2003).
- 513 26 Zanetti, G. *et al.* The structure of the COPII transport-vesicle coat assembled on membranes.  
514 *Elife* **2**, e00951, doi:10.7554/eLife.00951 (2013).
- 515 27 Böhm, J. *et al.* Toward detecting and identifying macromolecules in a cellular context: Template  
516 matching applied to electron tomograms. *Proceedings of the National Academy of Sciences* **97**,  
517 14245-14250, doi:doi:10.1073/pnas.230282097 (2000).
- 518 28 de Teresa-Trueba, I. *et al.* Convolutional networks for supervised mining of molecular patterns  
519 within cellular context. *Nature Methods* **20**, 284-294, doi:10.1038/s41592-022-01746-2 (2023).
- 520 29 Moebel, E. *et al.* Deep learning improves macromolecule identification in 3D cellular cryo-electron  
521 tomograms. *Nature Methods* **18**, 1386-1394, doi:10.1038/s41592-021-01275-4 (2021).
- 522 30 Wu, S., Liu, G. & Yang, G. in *2022 IEEE 19th International Symposium on Biomedical Imaging*  
523 *(ISBI)*. 1-5.
- 524 31 Hao, Y. *et al.* VP-Detector: A 3D multi-scale dense convolutional neural network for  
525 macromolecule localization and classification in cryo-electron tomograms. *Computer Methods*  
526 *and Programs in Biomedicine* **221**, 106871, doi:<https://doi.org/10.1016/j.cmpb.2022.106871>  
527 (2022).
- 528 32 Rice, G. *et al.* TomoTwin: generalized 3D localization of macromolecules in cryo-electron  
529 tomograms with structural data mining. *Nature Methods* **20**, 871-880, doi:10.1038/s41592-023-  
530 01878-z (2023).
- 531 33 Balyschew, N. *et al.* Streamlined structure determination by cryo-electron tomography and  
532 subtomogram averaging using TomoBEAR. *Nature Communications* **14**, 6543,  
533 doi:10.1038/s41467-023-42085-w (2023).
- 534 34 Jimenez de la Morena, J. *et al.* ScipionTomo: Towards cryo-electron tomography software  
535 integration, reproducibility, and validation. *J Struct Biol* **214**, 107872,  
536 doi:10.1016/j.jsb.2022.107872 (2022).
- 537 35 Liu, H.-F. *et al.* nextPYP: a comprehensive and scalable platform for characterizing protein  
538 variability in situ using single-particle cryo-electron tomography. *Nature Methods*,  
539 doi:10.1038/s41592-023-02045-0 (2023).
- 540 36 Zheng, S. Q. *et al.* MotionCor2: anisotropic correction of beam-induced motion for improved cryo-  
541 electron microscopy. *Nat Methods* **14**, 331-332, doi:10.1038/nmeth.4193 (2017).
- 542 37 Kremer, J. R., Mastronarde, D. N. & McIntosh, J. R. Computer visualization of three-dimensional  
543 image data using IMOD. *J Struct Biol* **116**, 71-76, doi:10.1006/jsbi.1996.0013 (1996).
- 544 38 Zheng, S. *et al.* AreTomo: An integrated software package for automated marker-free, motion-  
545 corrected cryo-electron tomographic alignment and reconstruction. *Journal of Structural Biology*:  
546 *X* **6**, 100068, doi:<https://doi.org/10.1016/j.yjsbx.2022.100068> (2022).
- 547 39 Rohou, A. & Grigorieff, N. CTFFIND4: Fast and accurate defocus estimation from electron  
548 micrographs. *J Struct Biol* **192**, 216-221, doi:10.1016/j.jsb.2015.08.008 (2015).
- 549 40 Heumann, J. M., Hoenger, A. & Mastronarde, D. N. Clustering and variance maps for cryo-  
550 electron tomography using wedge-masked differences. *Journal of Structural Biology* **175**, 288-  
551 299, doi:<https://doi.org/10.1016/j.jsb.2011.05.011> (2011).
- 552 41 Hall, S. R. The STAR file: a new format for electronic data transfer and archiving. *Journal of*  
553 *Chemical Information and Computer Sciences* **31**, 326-333, doi:10.1021/ci00002a020 (1991).
- 554 42 Shimogawa, M. M. *et al.* FAP106 is an interaction hub for assembling microtubule inner proteins  
555 at the cilium inner junction. *Nature Communications* **14**, 5225, doi:10.1038/s41467-023-40230-z  
556 (2023).

- 557 43 Schur, F. K. M. *et al.* An atomic model of HIV-1 capsid-SP1 reveals structures regulating  
558 assembly and maturation. *Science* **353**, 506-508, doi:doi:10.1126/science.aaf9620 (2016).
- 559 44 von Kügelgen, A., Alva, V. & Bharat, T. A. M. Complete atomic structure of a native archaeal cell  
560 surface. *Cell Reports* **37**, 110052, doi:<https://doi.org/10.1016/j.celrep.2021.110052> (2021).
- 561 45 Pum, D., Breitwieser, A. & Sleytr, U. B. Patterns in Nature—S-Layer Lattices of Bacterial and  
562 Archaeal Cells. *Crystals* **11**, 869 (2021).
- 563 46 Liu, Y.-T. *et al.* Isotropic reconstruction for electron tomography with deep learning. *Nature*  
564 *Communications* **13**, 6482, doi:10.1038/s41467-022-33957-8 (2022).
- 565 47 Tan, A., Pak, A. J., Morado, D. R., Voth, G. A. & Briggs, J. A. G. Immature HIV-1 assembles from  
566 Gag dimers leaving partial hexamers at lattice edges as potential substrates for proteolytic  
567 maturation. *Proceedings of the National Academy of Sciences* **118**, e2020054118,  
568 doi:doi:10.1073/pnas.2020054118 (2021).
- 569 48 Guo, S., Saha, I., Saffarian, S. & Johnson, M. E. Structure of the HIV immature lattice allows for  
570 essential lattice remodeling within budded virions. *eLife* **12**, e84881, doi:10.7554/eLife.84881  
571 (2023).
- 572 49 Talledge, N. *et al.* HIV-2 Immature Particle Morphology Provides Insights into Gag Lattice  
573 Stability and Virus Maturation. *Journal of Molecular Biology* **435**, 168143,  
574 doi:<https://doi.org/10.1016/j.jmb.2023.168143> (2023).
- 575 50 Lasker, K. *et al.* The material properties of a bacterial-derived biomolecular condensate tune  
576 biological function in natural and synthetic systems. *Nature Communications* **13**, 5643,  
577 doi:10.1038/s41467-022-33221-z (2022).
- 578 51 Sleytr, U. B., Schuster, B., Egelseer, E. M. & Pum, D. S-layers: principles and applications. *FEMS*  
579 *Microbiol Rev* **38**, 823-864, doi:10.1111/1574-6976.12063 (2014).
- 580 52 Draganova, E. B. *et al.* The universal suppressor mutation in the HSV-1 nuclear egress complex  
581 restores membrane budding defects by stabilizing the oligomeric lattice. *bioRxiv*,  
582 2023.2006.2022.546118, doi:10.1101/2023.06.22.546118 (2023).
- 583 53 Wang, H. *et al.* Hierarchical organization and assembly of the archaeal cell sheath from an  
584 amyloid-like protein. *Nature Communications* **14**, 6720, doi:10.1038/s41467-023-42368-2 (2023).
- 585 54 Tegunov, D., Xue, L., Dienemann, C., Cramer, P. & Mahamid, J. Multi-particle cryo-EM  
586 refinement with M visualizes ribosome-antibiotic complex at 3.5 Å in cells. *Nature Methods* **18**,  
587 186-193, doi:10.1038/s41592-020-01054-7 (2021).
- 588 55 Meng, E. C. *et al.* UCSF ChimeraX: Tools for Structure Building and Analysis. *Protein Sci*, e4792,  
589 doi:10.1002/pro.4792 (2023).
- 590 56 Tan, Y. Z. *et al.* Addressing preferred specimen orientation in single-particle cryo-EM through  
591 tilting. *Nat Methods* **14**, 793-796, doi:10.1038/nmeth.4347 (2017).
- 592 57 Herrmann, J. *et al.* A bacterial surface layer protein exploits multistep crystallization for rapid self-  
593 assembly. *Proceedings of the National Academy of Sciences* **117**, 388-394,  
594 doi:doi:10.1073/pnas.1909798116 (2020).
- 595

596

## 597 **Figure Legends**

### 598 **Figure 1, Illustration of TomoNet's comprehensive pipeline for cryoET and STA.**

599 The pink border encloses the sequential functions implemented in TomoNet, and they can be  
600 subdivided into three principal segments, delineated by the orange borders. These segments  
601 include tomogram preparation on the left, template matching-based particle picking "Auto  
602 Expansion" in the center, and deep learning-based automatic particle picking on the right.

### 603 **Figure 2, A screenshot of TomoNet GUI.**

604 The TomoNet GUI contains three main areas: the menu bar (top left), the input and operate  
605 area (top right), and the log window (bottom). Bottom left: results generated by the "3D  
606 Subtomogram Place Back" function can be visualized in ChimeraX. Bottom right: intermediate  
607 results of picked particles viewed with IMOD.

### 608 **Figure 3, Illustration of the first two iterations of "Auto Expansion" particle picking.**

609 There are two patches of a hexagonal lattice with individual particles represented by solid  
610 hexagons. At iteration 0, 18 "candidate" particles (dashed blue) were selected from the  
611 neighbors of 3 "seed" particles (orange). 14 good particles remained and will serve as "seed"  
612 particles in iteration 1, and 3 "seed" particles in iteration 0 were saved in the final particle set  
613 (green). At iteration 1, 35 "candidate" particles were selected from the neighbors of 14 "seed"  
614 particles. 29 good particles remained and will serve as "seed" particles in iteration 2, and 14  
615 "seed" particles were saved in the final particle set. "Auto Expansion" is an iterative process and  
616 will stop when no "candidate" can be detected.

### 617 **Figure 4, Illustration of "AI AutoPicking" process consisting of three steps.**

618 The HIV dataset was used for this illustration, and the particles refer to Gag hexamers. **a**,  
619 Training dataset preparation. Using the user-provided tomograms with associated particle  
620 coordinate files, subtomograms containing particle densities were extracted. For each



621 subtomogram, TomoNet generated a segmentation map based on the coordinates of particles,  
622 where the voxels near a particle's center are shown as white and the others as black. **b**, Neural  
623 network training. The generated subtomograms and segmentation maps were used as the input  
624 and output to train the convolutional neural network in learning how to segment out particle  
625 densities. **c**, Particle coordinate prediction. Firstly, TomoNet applied the trained neural network  
626 model to unseen tomograms and generated associated predicted segmentation maps. Then,  
627 the particle coordinate information was obtained from the segmentation maps using clustering  
628 algorithms.

### 629 **Figure 5, TomoNet application to arrays of matrix protein in HIV VLPs.**

630 **a**, Illustration of picked “seed” particles on a spherical VLP. Green segments represent the  
631 particles' Y-axis. Scale bar is 20 nm. **b**, “Auto Expansion” result on three VLPs within tomogram  
632 TS\_01, with yellow dots representing the center of the hexamer subunits. **c**, “AI AutoPicking”  
633 particle prediction result of tomogram TS\_45 shows its ability to pick particles on all lattices of  
634 different sizes and shapes. **d**, Visualization of three different variations of the HIV Gag lattices  
635 generated by placing back averaged structures, two exhibiting a spherical shape, and one  
636 presented as a fragment. Blue arrows indicate defects in the lattice.

### 637 **Figure 6, Final map resolution of HIV Gag hexamer.**

638 **a**, Final reconstruction of Gag hexamer (grey) fitted with the atomic model (PDB: 5I93). **b**, One  
639 segmented Gag monomer structure, inset shows a closer view of carboxy-terminal domain  
640 overlay with the atomic model. **c**, Directional Fourier shell correlation (FSC) curves for the STA  
641 of Gag hexamer structure, with a global resolution at 3.2 Å.

### 642 **Figure 7, Comparative visualization of lattices obtained from TomoNet and Relion** 643 **tutorial.**

644 **a, b**, Visualized comparison of particles used in TomoNet and Relion tutorial within tomogram  
645 TS\_01. TomoNet can pick particles not only on a sphere-like lattice but also on others with  
646 random shapes. **c, d**, A comparison of particle picking results on two sphere-like shape VLPs  
647 from TomoNet and Relion tutorial. **e**, A zoom-in view of an irregularly shaped lattice. Coloring is  
648 based on surface curvatures at the point of each subunit.

649 **Figure 8, TomoNet application to S-layer structure in FIB-milled cellular sample.**

650 **a**, A tomographic slice view shows two *C. crescentus* cells in a FIB-milled lamella. **b**, Orthogonal  
651 slice views of the averaged density map generated in TomoNet, showing the hexagonal  
652 distribution of S-layer inner domains. Scale bar is 20 nm. **c**, Visualization of S-layer lattices  
653 generated by placing back hexamer subunit maps simulated from PDB: 6P5T. Coloring is based  
654 on surface curvatures at the center of each subunit.

655 **Figure 9, TomoNet application to *in vitro* assembled NEC-bound membrane.**

656 **a, b**, Tomographic slice views show a large NEC lattice; the insets show different views of NEC  
657 hexamer subunits. Scale bar is 20 nm. **c**, Orthogonal slice views of an averaged density map  
658 generated in TomoNet show that NEC hexamer subunits consist of UL31/UL34 heterodimers.  
659 Scale bar is 10 nm. **d**, Visualization of an NEC lattice generated by placing back averaged maps  
660 shows that the large vesicle is compressed into a disk-like shape. The compression caused by  
661 sample freezing stretched the lattice, making it flat and split at the air-water surface. Coloring is  
662 based on surface curvatures at the center of each subunit. **e**, Atomic model of the UL31/UL34  
663 heterodimers fits into the final averaged map, with all helices well resolved.

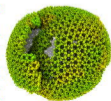
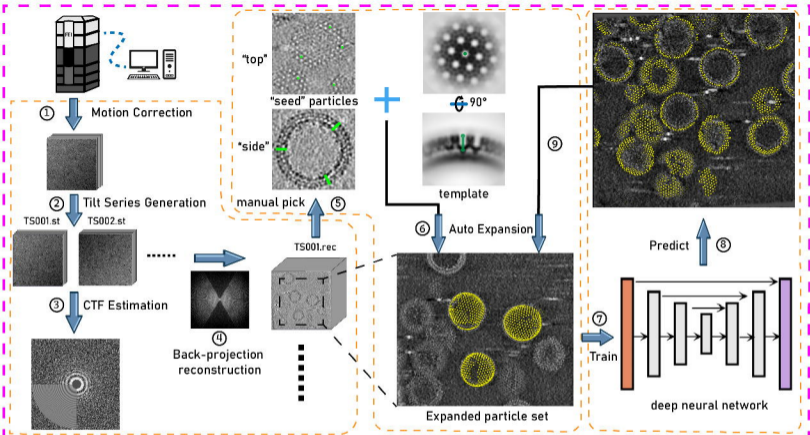
664

665 **Movie Legends**

666 **Movie 1, A spherical VLP consisting of hexamer Gag subunits, colored by local surface**

667 **curvature. “bad” particles with wrong alignment are shown as red.**

668 **Movie 2, A VLP lattice with irregular shape.**



11  
3D place back  
12  
particle clean

Export 16  
RELION  
4.0

Motion Correction

3D Reconstruction

CTF Estimation

Manual Picking

Auto Expansion

AI AutoPicking

Other Utilities

Generate tomograms.star

Generate Picking Parameter

Run Particle Expansion

Tomogram star file: /home/logicvay/Project/HIV/Expand/result\_from\_autopick/tomograms.star

Pick params file: /home/logicvay/Project/HIV/Expand/pick\_1030\_largerCCC.params

Select Expand Folder: /home/logicvay/Project/HIV/Expand/result\_from\_autopick

	Tomo Name	Rounds #	Final Particle #	Action	Action
1	01	16	5765	3dmod	Clean up
2	43	16	4043	3dmod	Clean up
3	45	18	5006	3dmod	Clean up
4	54	15	2838	3dmod	Clean up

Select Tomo Index: 1-4

Rounds: 10

Min Patch Size: 50

CPU #: 12

print cmd only 

RUN

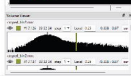
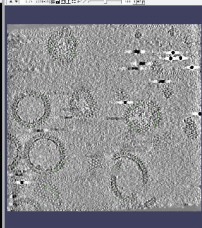
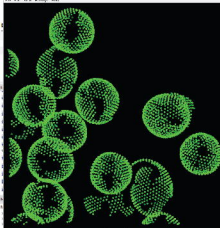
23-10-31 13:04:32 - INFO - Particle numbers 5295. After clean 4043! with 14 patches

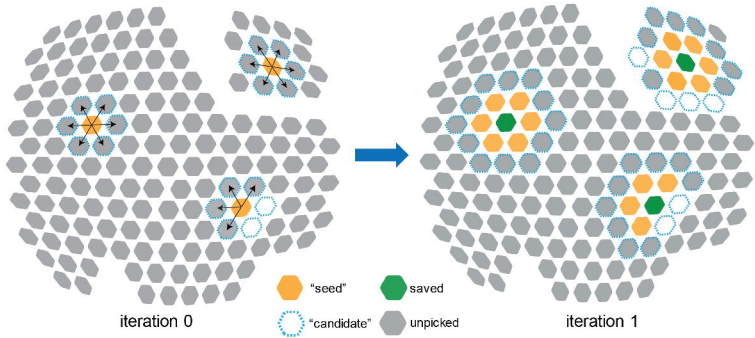
23-10-31 13:04:32 - INFO - The final coords and rotation are saved

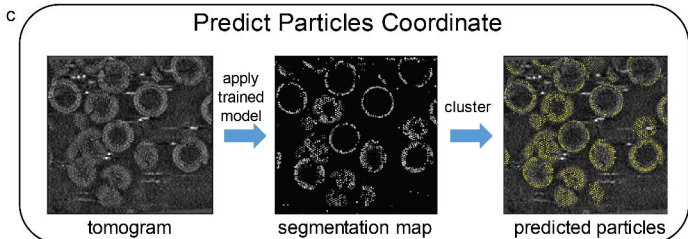
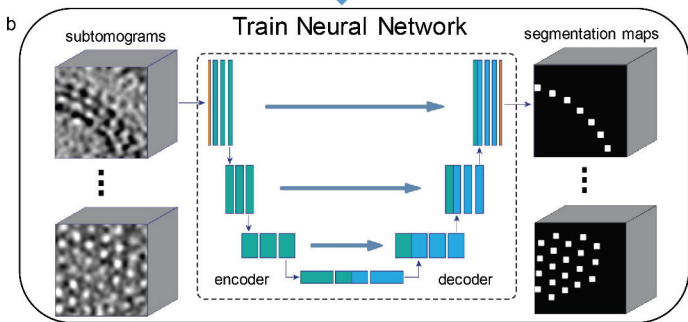
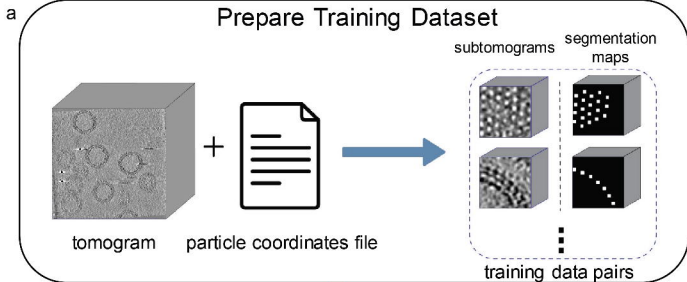
23-10-31 13:04:32 - INFO - Finish expand 43 for 0 rounds

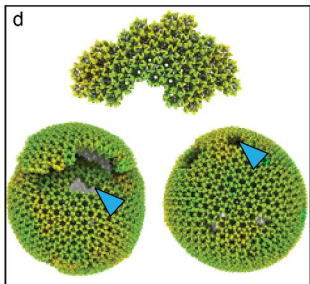
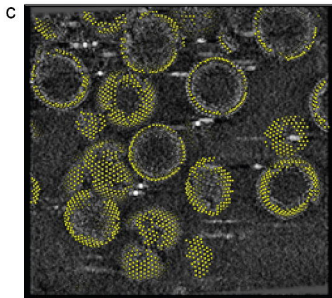
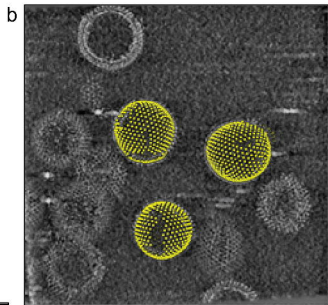
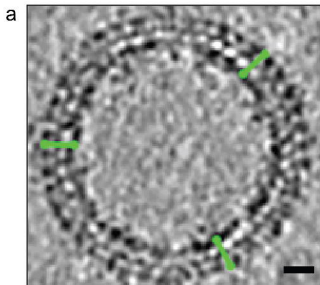
23-10-31 13:04:32 - INFO - Start expand 45 for 0 rounds

23-10-31 13:04:40 - INFO - Particle numbers 6761. After clean

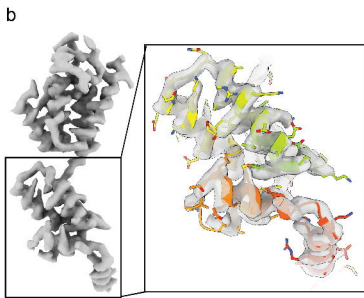
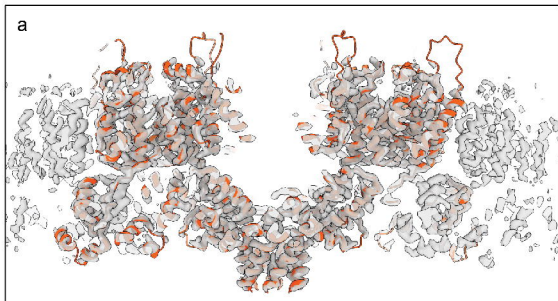












**c** Histogram and Directional FSC Plot  
Sphericity = 0.945 out of 1. Global resolution = 3.2 Å

